ACS APPLIED MATERIALS & INTERFACES

Research Article

www.acsami.org

# Toward Ultraflat Surface Morphologies During Focused Electron Beam Induced Nanosynthesis: Disruption Origins and Compensation

Robert Winkler,[†] Aleksandra Szkudlarek,[‡,§] Jason D. Fowlkes,[∥,⊥] Philip D. Rack,[∥,⊥] Ivo Utke,[‡] and Harald Plank*[,†,#]

[†]Graz Centre for Electron Microscopy, Steyrergasse 17, 8010 Graz, Austria

[‡]EMPA, Swiss Federal Laboratories for Materials Science and Technology, Laboratory for Mechanics of Materials and Nanostructures, Feuerwerkerstrasse 39, 3602 Thun, Switzerland

[§]AGH University of Science and Technology, Academic Centre for Materials and Nanotechnology, A. Mickiewicza 30, 30-059 Krakow, Poland

[∥]Center for Nanophase Materials Sciences, Oak Ridge National Laboratory, Oak Ridge, Tennessee 37831, United States

[⊥]Department of Materials Science and Engineering, University of Tennessee, Knoxville, Tennessee 37996, United States

[#]Institute for Electron Microscopy and Nanoanalysis, Graz University of Technology, Steyrergasse 17, 8010 Graz, Austria

Supporting Information

**ABSTRACT:** Emerging applications for nanoscale materials demand precise deposit shape retention from design to deposition. This study investigates the effects that disrupt high-fidelity shapes during focused electron beam induced nanosynthesis. It is shown that process parameters, patterning strategies and deposit topography can impose lateral precursor coverage gradients during growth resulting in unwanted topographic artifacts. The study classifies the evolving surface shapes into four general types and explains the formation and transition from a fundamental point of view. Continuum model calculations and simulations expand the experimental results to provide a comprehensive insight into understand the disruption mechanism. The findings demonstrate that the well-established concept of growth regimes has to be expanded by its lateral gradients as they strongly influence final shape fidelities. Finally, the study is complemented by a compensation strategy that improves the edge fidelity on the lower nanoscale to further push this technique toward the intrinsic limitations.

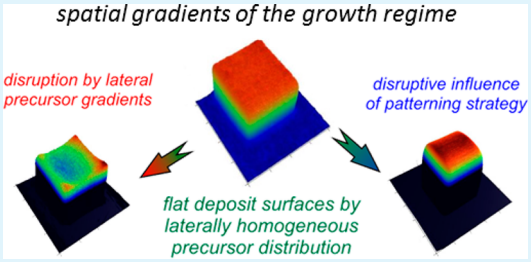


**KEYWORDS:** *focused electron beam induced deposition, patterning, morphology, platinum*

## 1. INTRODUCTION

Focused electron beam induced deposition (FEBID) relies on a highly localized nanosynthesis of functional precursor molecules via a nanometer sized, focused electron beam.[1−5] An injected gaseous precursor physisorbs on the specimen surface and is locally decomposed by an electron beam. Together with the very accurate and flexible positioning capabilities of the e-beam, FEBID represents a mask-less, additive direct-write method with spatial nanometer resolution, even on nonflat surfaces where classical resist based lithography is complicated or even impossible.[2,3,5−9] As different precursor chemistries provide a wide range of materials functionalities,[1,3] several application concepts have successfully been demonstrated including magneto-logics, storage or sensing[10,11] for magnetic deposits, strain sensors,[12] hall sensors,[13] and gas sensors.[14] While the long-lasting issue of unwanted carbon impurities in Co- and Pt-based deposits has recently been solved by different approaches,[9,15−20] topographic errors by means of missing flatness and/or edge sharpness still limits FEBID applications in which the morphology is an essential element (e.g., plasmonics, thin-film multilayer devices or high-resolution sensor gaps). Although progress has been made in the fundamental understanding of broadening effects which ultimately limits the achievable lateral resolution,[7,8,21−26] surface related aspects are rarely investigated with respect to its underlying mechanisms.[8,24] Such knowledge, however, is indispensable considering the industrial applications and their demand for predictable and reproducible shape fidelity on the lower nanoscale.

In this work, we therefore focus on the surface morphology of FEBID deposits, study disruption effects under different process conditions and link the experimental findings to lateral gradients in the precursor working regime. We demonstrate how surface morphologies of PtC deposits change as a function of process parameters, patterning strategies, and deposit thicknesses, leading to the identification of four basic morphologies. Continuum model calculations and finite difference simulations reveal that experimentally observed

Received: November 18, 2014
Accepted: January 15, 2015
Published: January 15, 2015





DOI: 10.1021/am508052k
ACS Appl. Mater. Interfaces 2015, 7, 3289−3297

surface shapes can consistently be rationalized by lateral gradients of the precursor coverage during growth. By that, it becomes evident that the well-established concept of the growth regime has to be expanded to account for, albeit subtle, lateral gradients as they strongly influences final shape fidelity. Based on this fundamental understanding, we finally introduce a compensation strategy that sharpens the edges of nanoscale deposits toward ultraflat, high-fidelity morphologies of FEBID structures, which we surmise are critical for many applications.

## 2. RESULTS

In the following, we start with the influence of the patterning strategy on the morphology. On the basis of the findings, we then use the most appropriate patterning type for a systematic study of other relevant FEBID process parameters. This results in the classification of four basic morphologies, which are described in detail and whose formation is explained in the Discussion section and rationalized with calculations and simulations.

**2.1. Patterning Strategy.** The considerations start with the influence of different patterning strategies, namely, raster (RA) and serpentine (SP) scanning. Atomic force microscopy (AFM) height images in Figure 1 reveal the morphologies for raster and serpentine strategies, which become apparent for the shortest dwell times (DT) and highest beam currents, as will be discussed in the next subsection. A chair-like morphology evolves for raster scanning with the highest features at the starting points of each scanning line (arrows). In contrast, serpentine strategies lead to a tunnel-like morphology in which lowest deposit heights evolve at the reversal points of the e-beam (arrows). A more detailed comparison of cross-sectional height profiles is shown in the following section. As discussed by Winkler et al.,[17] alternative patterning strategies by means of spiral-in (SI) or spiral-out (SO) can be used; however, they lead to diagonal features (trench and ridge) at the turning point of the e-beam (Supplement 1, Supporting Information) and are therefore not suitable alternatives when aiming for flat surfaces. Considering the unfavorable lateral asymmetry of raster patterns (Figure 1a) further experiments have been conducted with serpentine patterning strategies as the most promising candidate toward flat deposit surfaces.

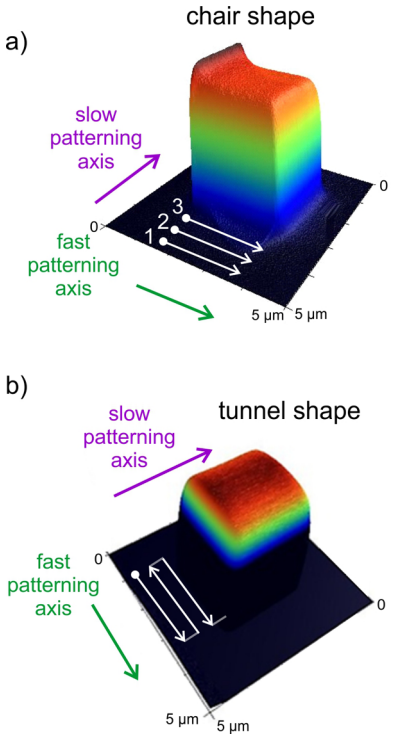


**Figure 1.** 3D-AFM height images of FEBID deposits fabricated via (a) raster and (b) serpentine patterning strategies resulting in chair- and tunnel-like morphologies, respectively. Both deposits were fabricated at 5 keV, 1600 pA, 1 $\mu$s dwell time, and 13 nm point pitch via 1000 patterning loops. The white arrows indicate the patterning sequence that defines the fast and slow patterning axes as indicated.

**2.2. Patterning Parameters.** Serpentine patterning was investigated over the processing range of beam current (25−6300 pA) and pixel dwell times (1−1000 $\mu$s) while the point pitch was kept constant at 13 nm. To provide constant total exposure times for each patterning pixel, we compensated decreasing DTs with an increasing number of patterning loops. On the basis of detailed AFM investigations, we divided the evolving surface morphologies into four different types for the investigated parameter space, as summarized in Figure 2: (1) flat, (2) concave, (3) slanted, and (4) patterning dependent. Representative 3D AFM height images are also shown to give a qualitative impression of the evolving morphologies. Note: The transition between these classifications varies, and the AFM images reveal the most pronounced results. In the following, a more detailed morphological description is given for all four types.

As a starting point, we consider the flat morphology (green range in Figure 2), which strongly suggests a steady-state precursor coverage gradient during patterning. As shown in the AFM height cross sections in Figure 3a, the deposits exhibit a fairly flat surface along the fast (parallel to the scan direction) and slow (orthogonal to the scan direction) patterning axes, as schematically shown in Figure 3e together with the gas flux direction.[17,27] The only deviations from an ideal situation are the nonvertical sidewall slopes and, in particular, the rounded upper edges. As discussed by Schmied et al.[24] and Arnold et al.[8] the former relies on a complex interplay between back- and forward scattered electrons from the substrate and the deposit itself. The latter, however, can be compensated toward sharper edges, as will be discussed later.

When the DTs were lowered, a concave shape evolved, as shown by a representative 3D AFM image in Figure 2 (yellow) and by AFM height cross sections in Figure 3b. Detailed analyses revealed the corners as the highest heights, edges as the intermediate heights, and central areas as the lowest heights that form the concave shape. Central cross-sectional profiles reveal no difference between fast and slow scan axes, as can be seen by essentially identical profiles in Figure 3b. As described in literature based on experiments, calculations, and simulations, it is well-known that lowest DTs lead to the lowest local precursor consumption and by that to the smallest lateral concentration gradients and low proximity depletion.[8,25,26,28,29] Intuitively, such a situation should then lead to most flat surfaces, which contradicts the observed concave shapes. However, it has to be kept in mind that very short DTs imply very short loop times, which strongly decreases the replenishment times in between two consecutive pulses at the same patterning pixel. This circumstance ultimately induces a lateral precursor gradient reflected by the concave morphology, as will be explained in detail in the Discussion section.


DOI: 10.1021/am508052k
ACS Appl. Mater. Interfaces 2015, 7, 3289−3297

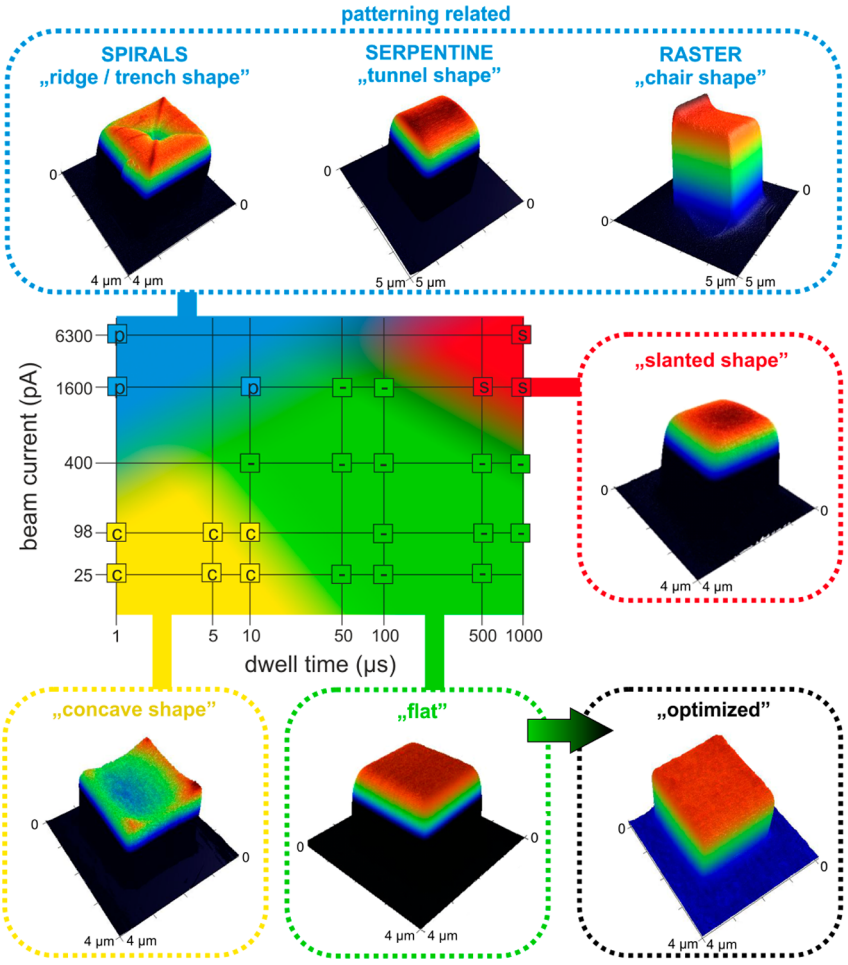


**Figure 2.** Classification of the morphology types obtained for serpentine/raster/spiral as a function of pixel dwell time (*x* axis) and beam current (*y* axis) for constant total exposure times at a primary electron energy of 5 keV: (green) flat, (yellow) concave, (red) slanted, and (blue) patterning related, which change shapes depending on the strategy used. AFM height images give a visualization of the four morphology types for the most illustrative parameter sets. (Bottom right) Representative image of a fully optimized patterning strategy within the flat regime (detailed explanation can be found in the main text).

In contrast, for very high beam currents and long dwell times (red area in Figure 2) a slanted morphology evolves. As evident by the AFM cross-sectional profiles in Figure 3c, the slant evolves only in the slow patterning axis (solid red), while widely flat surfaces are found along the fast patterning axis (dashed blue). Also, as evident on the right-hand side of the red cross-sectional profile and in the representative 3D AFM height image at the center (arrow) the final front is not as steep and smooth as the other three slopes. A similar effect has been reported for decreasing point pitches by van Dorp et al.,[30] who attributed this feature to enhanced secondary electron emission at the front slopes, which then increase the deposition rates, leading to ascending morphologies. Considering the very high beam currents, which entail higher local depletion, we expand this interpretation and suggest forward scattered electrons due to the thick deposits as discussed in detail later. Note: To rule out the influence of gas flux direction, we systematically rotated the pattern. The results revealed the slant is independent of the gas flux (Supplement 3, Supporting Information) which further supports the assignment to a FSE/SE-III related effect.

Finally, we again consider the blue range in Figure 2, which shows very different morphologies for different patterning strategies as discussed in the previous subsection. Here, we only discuss the most promising serpentine strategy within the investigated parameter space (details for raster strategy are in Supplement 5, Supporting Information). As can be seen by AFM height cross sections in Figure 3d, the surface is widely flat in the slow patterning direction (solid red) but strongly rounded at both edges along the fast patterning direction (dashed blue) which ultimately forms the tunnel shape (see representative 3D AFM inset). The dynamic evolution of this morphology is related to the turning points of the e-beam at the pattern edges as discussed in detail in the following section.

## 3. DISCUSSION

To correlate the experimentally found surface morphologies with lateral precursor gradients, we first need to consider different mechanisms of precursor replenishment during growth, following the notation and explanation by Winkler et al.[17] Three main components are involved in the local precursor replenishment for each patterning pixel: (1) gas flux replenishment (GFR) which is laterally constant, (2) surface diffusion replenishment from the deposit (SDR-D) following gas flux adsorption on the deposit surface, and (3) surface diffusion replenishment from the surrounding substrate (SDR-S). The two SDR components differ in that SDR-D components rely on the GFR contribution after local depletion due to the e-beam pulse while the surrounding substrate is


DOI: 10.1021/am508052k
ACS Appl. Mater. Interfaces 2015, 7, 3289−3297

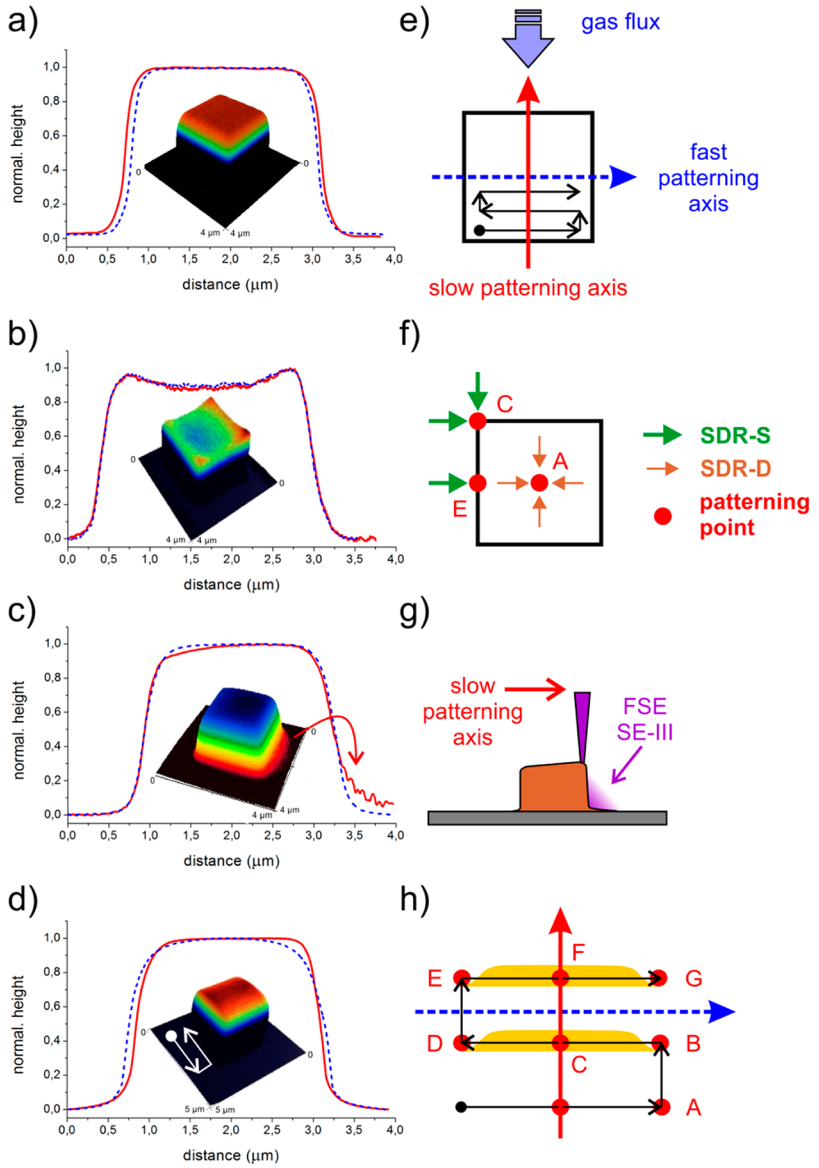


**Figure 3.** AFM height cross sections for (a) flat, (b) concave, (c) slanted, and (d) tunnel shapes, together with (insets) representative AFM 3D images. (e) Pattern footprint (black square) together with the serpentine strategy (black arrows) relative to the gas flux direction. The dashed blue and solid red lines indicate the directions of the AFM height cross sections along the fast and slow patterning axis, respectively, valid for all graphs in this figure. (f) Schematic representation of the different precursor adsorbate supply directions for surface diffusive replenishment (SDR) split into deposit related SDR-D and substrate related SDR-S components for three different patterning points (see text for details). (g) Scheme illustrating the deposit cross section and (purple) scanning e-beam and FSE/SE-III contributions leading to proximity growth,[8,24] as discussed in the text and simulated in Figure 4d. (h) Scheme illustrating the patterning process in detail for several pixel positions (red points) to explain the tunnel shape via different replenishment degrees, as indicated by the yellowish bars for two scan lines (see text for details).

unexposed, hence, having a higher virtually constant equilibrium coverage. Therefore, depending on the local depletion degree, SDR-S components (from outside the deposit) can be stronger than SDR-D contributions (from the deposit area itself) during replenishment. Furthermore, as shown by Winkler et al.[17] in detail, the slow patterning direction with respect to the incoming gas flux direction is essential.[17,27,31]

With this framework, we consider the four basic morphologies together with related patterning parameters and reveal, in conjunction with calculations and simulations, how laterally varying precursor regimes disrupt the intended surface morphology.

**3.1. Surface Shapes.** As a starting point, the flat morphologies are reconsidered and strongly suggest lateral homogeneous precursor coverage due to a local equilibrium between depletion and GFR, SDR-D, and SDR-S. For very short DTs, the dynamic situation during growth has to be considered. During the first patterning loop, a certain degree of local depletion occurs. While the gas flux replenishment component is constant, surface diffusion toward subsequently exposed patterning pixel plays an essential role as schematically shown in Figure 3f. For an edge point E the SDR-S component is stronger than the SDR-D component as the former supply path stem from unexposed, higher coverage regions. In contrast, a central patterning point A (Figure 3f) can mainly be replenished by GFR and SDR-D components due to the large distance from the substrate source (1 $\mu$m). Taking into account the short refresh times due to short DTs, it becomes


DOI: 10.1021/am508052k
ACS Appl. Mater. Interfaces 2015, 7, 3289−3297

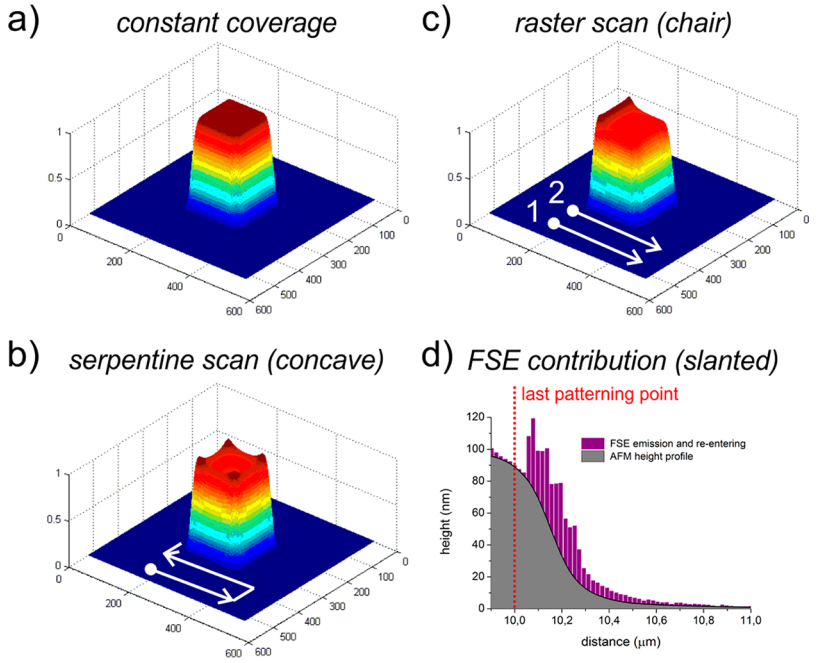


**Figure 4.** (a) Continuum model calculations of a raster/serpentine scanning strategy imposing a constant surface coverage of precursor adsorbates over time and position: a flat surface is obtained for both patterning strategies. Subsequently, surface diffusion was enabled together with raster (c) and serpentine strategy (b) revealing the chairlike and concave shapes, respectively, as experimentally observed (see Figure 3). (d) Monte Carlo simulations of electron trajectories (5 keV primary electrons) for real deposit shape (AFM profile in gray) and material (typical $PtC_5$ composition). The purple bars indicate exiting and re-entering FSE contributions (entailing SE-IIIs), as suggested for the slanted morphologies (arbitrary intensity scale). The far-reaching proximity deposition is then expected to increase the base level on which subsequent deposition along the slow patterning axis takes place leading to the ascending morphologies shown in Figure 3c for the slanted shape.

evident that the edge point E has a higher coverage and consequently a higher volume growth rate due to the stronger SDR-S component compared to central SDR-D contributions. This situation becomes even more dominant at corner points C (Figure 3f), as there are two different SDR-S directions that contribute compared to a single directional supply at point E. Cumulatively, this explains the concave shape shown in the representative 3D AFM inset in Figure 3b. To further support these assumptions, the continuum model has been used to simulate the results.[32,33] First, constant precursor coverage over time and position has been assumed during patterning leading to flat surfaces, as shown in Figure 4a. Then, dynamic depletion and surface diffusion were enabled, which lead to concave shapes for the shortest DTs, as representatively shown in Figure 4b, in agreement with experimental findings. Increasing DTs during the experiments (right-hand shift in Figure 2) lead to increased refresh times and improve the local replenishment situation for each patterning point resulting in flat surfaces.

In contrast, when using short DTs but higher beam currents (upward direction in Figure 2) the volumetric growth rates also increase. The higher deposits have then to be considered as morphological barrier which complicates the diffusion via substrate related SDR-S paths (average diffusion lengths have been estimated to be <25 nm via simulations in Winkler et al.[17] in agreement with previous work by Alkemade et al.[34,35]). Consequently, the SDR-S component decreases at increasing deposit heights and deposit related SDR-D contributions dominate which finally lead to the tunnel shapes as discussed later. Therefore, it can be concluded that the evolving concave shape is a consequence of short refresh times and site specific precursor gradients due to the different replenishment components (SDR-S at edges/corners versus SDR-D for central areas). Experiments (short DTs, low beam currents) with deposit heights above the average diffusion lengths[17] still show the concave shape, which is attributed to the fact that once the concave shape evolved during early growth, it is mimicked for further growth. By that, the experimentally observed concave height morphology can be understood as a direct visualization of lateral precursor gradients at such patterning conditions. This demonstrates that for the highest shape retention the classically used concept of the growth regime has to be expanded to account for the lateral distribution as subtle gradients impact the final morphology.

Next, the slanted morphology at highest DTs and beam currents is considered (red area in Figure 2). As shown by Winkler et al.[17] such patterning conditions lead to strong local depletion and an excess number of electrons (molecule limited regime). Also, it has to be considered that the pixel growth rate is high leading to deposit heights above the average diffusion lengths.[17] Consequently, the growth front is predominantly replenished by the gas flux and SDR-D related downward diffusion leading to lower growth efficiencies compared to situations where SDR-S components are strongly contributing.[17] Based on quantitative AFM data, Monte Carlo electron scattering simulations have been conducted to investigate the surface flux of forward scattered electrons (FSE). Figure 4d shows the AFM height profile (gray) with emitted and re-entering FSEs as purple overlay together with the last patterning point indicated by the dashed vertical line. On one hand, these FSE are expected to directly contribute to the dissociation process, on other hand they trigger a cascade of secondary electrons (defines as SE-III) which are assumed to be the predominant dissociation species due to their relatively higher dissociation cross-section.[36−38] As discussed in detail by


DOI: 10.1021/am508052k
ACS Appl. Mater. Interfaces 2015, 7, 3289−3297

Schmied et al.[24] these FSE contributions not only leads to a broadening of the deposit slope but also to a FSE related proximity deposition since re-entering FSEs impact substrate areas where all replenishment components (GFR, SDR-S) provide comparable high precursor coverage. Hence, as shown by the scheme in Figure 3g, FSE/SE-III contributions (purple shades) lead to deposit growth outside the scanning pattern. Subsequent patterning rows then start on higher base levels which ultimately lead to the ascending deposit heights along the slow patterning direction as schematically shown in Figure 3g (brown box). Further evidence comes from final cross sections (solid red line in Figure 3c), which show higher structures on the front end also recognizable in the representative 3D AFM inset. This explanation is further consistent with the fact that this effect should only be dominant for a high number of (unconsumed) FSEs which require high beam currents and long DTs in agreement with the parameter map in Figure 2 (see also Supplement 3, Supporting Information). The main point of this section is the finding that lateral precursor gradients can result in excessive deposition at deposit slope via electron emission (FSE/SE-III) and entailed re-entry which leads to unwanted proximity deposition.

Finally, the patterning dependent morphologies need to be discussed which evolve for low-to-medium DTs and medium-to-high beam currents (blue region in Figure 2). First, the raster scan is considered which leads to a chair like morphology as shown in Figure 1a. It is well-known that the local depletion increases with DT on a single pixel.[1] This, in turn, induces a concentration gradient in the beam proximity, which initiates surface diffusion toward the exposed patterning pixel. As demonstrated by Plank et al.[26] the radius of this concentration gradient can reach 100 nm for deposition parameters according to the blue range in Figure 2. This implies that subsequent patterning points start at slightly depleted areas, which reduce the volume growth rate. Expanding this concept along a single scan line, the growth rate continuously decays until it reaches a nonzero steady-state situation governed by GFR and SDR-D components. If the line scan is long enough, (indicated by arrows in Figure 1a) the starting point of consecutive lines are not affected by proximity related depletion as it is fully replenished during the line scan. Again, this chairlike morphology directly reflects the transient behavior of the precursor coverage during each line scan where it is initially high at the beginning of the line and decays to a steady state value. To investigate this assumption via calculations, we again used the continuum model. Figure 4c shows the result in which the chair like feature on the left-hand side is clearly evident (see patterning directions at the bottom). The decay length, however, should be a function of the DT (and current) because longer beam pulses should establish steady state conditions during the first patterning points. This has been verified by additional experiments together with its dependence on the gas flux direction (Supplement 2, Supporting Information) which, together with the calculations, support the explanation for chair like surface shapes.

When changing the patterning strategy from raster to serpentine at same parameters, the morphology changes into tunnel shapes, as shown in Figure 1b. Figure 3d gives the associated cross-sectional profiles along the slow and fast patterning direction revealing the downward bent characteristics only for the fast scan axis (compare to the 3D AFM inset and the arrows). To explain this behavior, we must consider the dynamically changing SDR-S: due to the high beam currents, the deposit heights in the range of 100 nm exceed the average diffusion lengths which minimize SDR-S as replenishment components.[17] This implies that the volume growth rate at the line ends (path from point C to D in Figure 3h) decays, as experimentally observed. In contrast, the SDR-D still delivers precursor molecules as the replenishment of every deposit plateau after every loop as the GFR stays constant. Additionally, we condsider the different replenishment situation for subsequently patterned points E and F in Figure 3h: while point E is strongly depleted due to the quasi-stationary beam movement at the reversal point (D → E), point F has more time to be replenished by GFR and SDR-D components, further increasing the central volume growth rates. Both effects together lead to lower surface coverage at the reversal points (indicated by the yellow bars), leading to downward bent side walls parallel to slow patterning axis as experimentally observed (blue line and 3D AFM image in Figure 3d). When reducing the beam current at short DTs, the tunnels are shaped into concave morphologies as expected. This can be explained by the reduced deposits heights that enable SDR-S components to contribute, which first balances the tunnel shapes and then dominates the situation toward concave shapes, as experimentally observed.

The most important finding from this section is the concept that growth regimes necessarily has to be expanded to include evolving lateral gradients. This not only has strong impact on the surface morphology as discussed above, but it is also expected to have implications on the lateral chemistry and functionality as it is strongly connected to local growth regimes.[39,40] From a practical point of view, we can state that the most beneficial patterning strategy seems to be the serpentine approach which, within the right parameter range, provides extremely flat surfaces, however, with rounded edges. The latter aspect is discussed in the following section, including a compensation strategy based on the fundamental understanding derived above.

**3.2. Edge Effect Correction in Flat Shape Exposure Conditions.** As outlined in the previous section, flat shapes are obtained by achieving laterally homogeneous precursor coverage due to a local equilibrium between depletion and GFR, SDR-D, and SDR-S. Consequently, we can refer to the knowledge of classical resist-based e-beam lithography[41,42] to address any shape deviations, especially to improve the sharpness of round edges due to proximity effects. As discussed in detail by Schmied et al.,[24] the side walls of a FEBID deposit show a symmetrically increasing/decreasing slope around the edge patterning points as schematically indicated in Figure 5b,c. Careful correlation revealed the lateral expansion of the upper edge rounding toward a constant height in good agreement with the backscatter electrons (BSE) radius of about 100 nm in typical $PtC_5$ deposits.[8,24] Similar to the FSE discussion, it has to be noted that we assume BSE-related secondary electrons type II (SE-II) as the predominant dissociation species and BSE only as predominant trigger-electrons, although a certain contribution via direct BSE dissociation is also assumed. To explain the rounded top edge, we consider different patterning points, as shown by the scheme in Figure 5a. The growth rate for a central point is given by (1) direct exposure at this point and (2) by BSE/SE-II contributions from surrounding areas according to the BSE radius within the deposit. However, the growth rate of edge points consists only from its direct exposure and BSE/SE-II support from the inner areas meaning ∼38% decay of BSE/SE-II contributions. The situation is even


DOI: 10.1021/am508052k
ACS Appl. Mater. Interfaces 2015, 7, 3289−3297

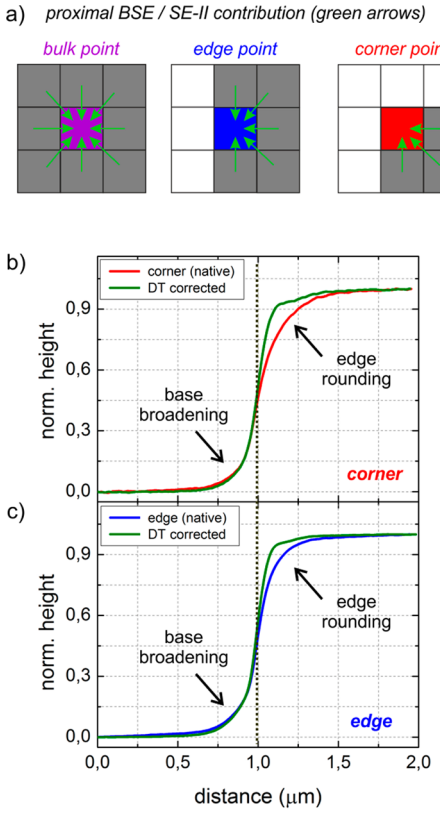


**Figure 5.** Illustration of edge-sharpness improvement within flat shape exposure conditions. (a) Schematic top view showing the proximity effect due to BSE/SE-II contributions from surrounding deposit areas for (left) bulk, (center) edge, and (right) corner points, which illustrate that missing neighbors lead to reduced volume growth rates at edge and corner patterning points. The real edge profiles (AFM cross sections) are shown in (b, red line) corner points and (c, blue line) edge points; (b and c, green curves) improvements in edge sharpness can be achieved by applying additional dwell time for patterning points close to the edges (within the BSE radius in $PtC_5$). However, the base broadening effects are a convolution of substrate related BSE/SE-II and deposit related FSE contributions, which cannot be compensated by the given strategy.[8,24]

worse for corner points in which ~63% of the BSE/SE-II contribution gets lost (details are in Supplement 4, Supporting Information) compared to central patterning points. Figure 5b,c show AFM height cross sections across a corner and an edge by red and blue curves, respectively. As can be seen, the edge rounding for corners is highest as expected due to the above-mentioned explanation. However, this lack of dissociating electrons at edges and corners can be corrected by dynamic DT adaption. The result of such a compensation strategy is also shown in Figure 5b and considerably minimizes the edge sharpness and supports the model above. The base broadening, however, is a complex process between substrate related BSE/SE-II and FSE/SE-III,[8,24] which cannot be compensated by the DT approach. Note that independent of the position or compensation, the outer tails are always similar. Hence, the introduced compensation allows sharpening of upper edges and corners but cannot be used for reducing the base broadening. The latter can only be reduced by highest primary energies as shown in detail by Schmied et al.[24] Please note, despite the strong improvement based on simple calculations (Supplement 4, Supporting Information) we consider a simulation based compensation approach as most promising as it can account for different situations such varying deposit footprints or smaller heights where the vertical expansion of the interaction volume can change the situation. Such simulation and experimental compensation strategies with electron beam parameter adaptations and gas flux vector contributions will be elaborated in a future work.

## 4. CONCLUSION

In conclusion, we have demonstrated how the surface morphology changes as a function of lateral precursor gradients, induced by varying dwell times and beam currents. We could classify the shapes in four different types: (1) flat, (2) concave, (3) slanted, and (4) patterning dependent. The latter can be further categorized into different shapes such as trenches, chairlike, and tunnel-shapes for spiral, raster, and serpentine scanning, respectively. The serpentine patterning strategy turned out to be most symmetric and predictable in terms of generating flat-top surface morphologies. Although the flat regime provides sufficiently homogeneous surface properties, the edges and corners are always found to be rounded which, together with previous studies, is suggested to originate from backscattered electrons of the deposit. However, we successfully demonstrated an edge-correction approach, which considerably enhances edge and corner sharpness. Together with previous studies, we can summarize some major effects that disrupt ideal surfaces: (1) gas flux effects, avoidable;[17] (2) surface curvature, avoidable (this study); (3) edge rounding, compensable (this study); and (4) base broadening, minimizable.[7,21,24] The main aspect of this study, however, is the fact that lateral precursor gradients are responsible for the observed deviations from ideally flat surfaces. Also, despite the fact that lowest beam currents and shortest dwell times have often been considered ideal, as it promotes the electron limited regime, the study demonstrated that lateral precursor gradients have strong implications and can lead to nonideal results. Therefore, the well-established concept of the growth regime has to be expanded to include possible subtle lateral gradients to exploit the full potential toward high fidelity shapes for real FEBID applications.

## 5. METHODOLOGY

All FEBID deposits were fabricated with a NOVA 200 dual beam system (FEI, The Netherlands) using MeCpPt(IV)$Me_3$ precursor in combination with a standard FEI gas injection system (GIS) having inner and outer diameters of 500 and 830 $\mu$m, respectively. The GIS was tilted by 52° with respect to the sample surface and placed at a vertical distance of 180 ± 10 $\mu$m with the long GIS main axis arranged in a lateral distance of 200 ± 10 $\mu$m with respect to the deposition area as described in detail in [17]. Si samples with an area of 10 × 10 mm and with 3 nm $SiO_2$ (see reference 16) were used and prepared in a laminar flow box for experiments. After immediate transfer of the samples to the dual beam microscope chamber, a background pressure of at least $9 \times 10^{-6}$ mbar was established before any experiment was conducted.

After beam focusing in the eucentric height (5 mm), the stage was moved to the deposition area (blanked e-beam) and then rested for at least 15 min to minimize mechanically induced stage drift. The precursor was preheated to 45 °C for at least 30 min prior to any experiments and opened for at least 3 min prior to any deposition to provide equilibrium surface coverages. All experiments in this study have been performed at 5 keV primary energies and a pixel distance (point pitch) of 13 nm. The electron beam movement was controlled via stream files, generated with Matlab (release 2010b, MathWorks, U.S.) and double checked on errors in the point sequence. After successful deposition the structures were characterized via Atomic


DOI: 10.1021/am508052k
ACS Appl. Mater. Interfaces 2015, 7, 3289−3297

force microscopy (AFM) performed with a Dimension 3100 microscope (Bruker AXS, Billerica, MA) operated with a Nanoscope IVa controller and equipped with a XYZ Hybrid scan head using Olympus OMCL TS-160/TS-240 cantilever in tapping mode. AFM tip convolution plays a negligible role at upper edges/corners due to comparable large curvatures (>20 nm in XY; < 10 nm in Z) compared to the AFM tip radii of about 5 nm. At deposit side walls, tip convolution only plays a role for deposits above 100 nm thickness, leading to slight overestimation of deposit base widths. However, as morphological effects on the deposit surface were the main focus of the study, the latter influences are of minor relevance. Analyses were performed using NanoScope Analysis software (v1.4, Bruker AXS, Billerica, MA) and Gwyddion (v2.37). A detailed description of the continuum model calculations and finite difference simulation is given in reference 17.

## ■ ASSOCIATED CONTENT

### Supporting Information

Morphological features obtained by using spiral patterning strategies; independency of chairlike and slanted morphologies on the directed gas flux; details of dwell time correction at edges and corners to minimize the top edge rounding effect; and deposit morphology evolution for raster and spiral patterning in dependency on dwell times and beam currents. This material is available free of charge via the Internet at http://pubs.acs.org.

## ■ AUTHOR INFORMATION

### Corresponding Author

*E-mail: harald.plank@felmi-zfe.at. Tel: +43 316 873 8821.

### Notes

The authors declare no competing financial interest.

## ■ ACKNOWLEDGMENTS

R.W. and H.P. gratefully acknowledge the valuable support provided by Prof. Dr. Ferdinand Hofer, DI Roland Schmied, DI Barbara Geier, DI Angelina Orthacker, DI Thomas Ganner, Ulrich Haselmann, Georg Arnold, and Martina Dienstleder. R.W. and H.P. also acknowledge financial support by the COST action CELINA (No. CM1301) and the EUROSTARS project TRIPLE-S (No. E! 8213). P.D.R. and J.D.F. acknowledge that their contributions were supported by the Center for Nanophase Materials Sciences, which is sponsored at Oak Ridge National Laboratory by the Scientific User Facilities Division, Office of Basic Energy Sciences, U.S. Department of Energy.

## ■ REFERENCES

(1) Utke, I.; Russell, P. E. *Nanofabrication Using Focused Ion and Electron Beams: Principles and Applications.*; Oxford University Press: New York, 2012.

(2) Van Dorp, W. F.; Hagen, C. W. A Critical Literature Review of Focused Electron Beam Induced Deposition. *J. Appl. Phys.* **2008**, *104*, 081301.

(3) Botman, a; Mulders, J. J. L.; Hagen, C. W. Creating Pure Nanostructures from Electron-Beam-Induced Deposition Using Purification Techniques: A Technology Perspective. *Nanotechnology* **2009**, *20*, 372001.

(4) Van Dorp, W. F.; Hansen, T. W.; Wagner, J. B.; De Hosson, J. T. M. The Role of Electron-Stimulated Desorption in Focused Electron Beam Induced Deposition. *Beilstein J. Nanotechnol.* **2013**, *4*, 474−480.

(5) Randolph, S. J.; Fowlkes, J. D.; Rack, P. D. Focused, Nanoscale Electron-Beam-Induced Deposition and Etching. *Crit. Rev. Solid State Mater. Sci.* **2006**, *31*, 55−89.

(6) Utke, I.; Hoffmann, P.; Melngailis, J. Gas-Assisted Focused Electron Beam and Ion Beam Processing and Fabrication. *J. Vac. Sci. Technol., B: Microelectron. Nanometer Struct.—Process., Meas., Phenom.* **2008**, *26*, 1197.

(7) Hari, S.; Hagen, C. W.; Verduin, T.; Kruit, P. Size and Shape Control of Sub-20 Nm Patterns Fabricated Using Focused Electron Beam-Induced Processing. *J. Micro/Nanolithogr., MEMS, MOEMS* **2014**, *13*, 033002.

(8) Arnold, G.; Timilsina, R.; Fowlkes, J. D.; Orthacker, A.; Kothleitner, G.; Rack, P. D.; Plank, H. Fundamental Resolution Limits during Electron Induced Direct Write Synthesis. *ACS Appl. Mater. Interfaces* **2014**, *6*, 7380−7387.

(9) Mehendale, S.; Mulders, J. J. L.; Trompenaars, P. H. F. A New Sequential EBID Process for the Creation of Pure Pt Structures from MeCpPtMe3. *Nanotechnology* **2013**, *24*, 145303.

(10) Gavagnin, M.; Wanzenboeck, H. D.; Belić, D.; Bertagnolli, E. Synthesis of Individually Tuned Nanomagnets for Nanomagnet Logic by Direct Write Focused Electron Beam Induced Deposition. *ACS Nano* **2013**, *7*, 777−784.

(11) Gabureac, M.; Bernau, L.; Utke, I.; Boero, G. Granular Co−C Nano-Hall Sensors by Focused-Beam-Induced Deposition. *Nanotechnology* **2010**, *21*, 115503.

(12) Huth, M.; Porrati, F.; Schwalb, C.; Winhold, M.; Sachser, R.; Dukic, M.; Adams, J.; Fantner, G. Focused Electron Beam Induced Deposition: A Perspective. *Beilstein J. Nanotechnol.* **2012**, *3*, 597−619.

(13) Gabureac, M. S.; Bernau, L.; Boero, G.; Utke, I. Single Superparamagnetic Bead Detection and Direct Tracing of Bead Position Using Novel Nanocomposite Nano-Hall Sensors. *IEEE Trans. Nanotechnol.* **2013**, *12*, 668−673.

(14) Kolb, F.; Schmoltner, K.; Huth, M.; Hohenau, A.; Krenn, J.; Klug, A.; List, E. J. W.; Plank, H. Variable Tunneling Barriers in FEBID Based PtC Metal-Matrix Nanocomposites as a Transducing Element for Humidity Sensing. *Nanotechnology* **2013**, *24*, 305501.

(15) Plank, H.; Noh, J. H.; Fowlkes, J. D.; Lester, K.; Lewis, B. B.; Rack, P. D. Electron-Beam-Assisted Oxygen Purification at Low Temperatures for Electron-Beam-Induced Pt Deposits: Towards Pure and High-Fidelity Nanostructures. *ACS Appl. Mater. Interfaces* **2014**, *6*, 1018−1024.

(16) Geier, B.; Gspan, C.; Winkler, R.; Schmied, R.; Fowlkes, J. D.; Fitzek, H.; Rauch, S.; Rattenberger, J.; Rack, P. D.; Plank, H. Rapid and Highly Compact Purification for Focused Electron Beam Induced Deposits: A Low Temperature Approach Using Electron Stimulated $H_2O$ Reactions. *J. Phys. Chem. C* **2014**, *118*, 14009−14016.

(17) Winkler, R.; Fowlkes, J.; Szkudlarek, A.; Utke, I.; Rack, P. D.; Plank, H. The Nanoscale Implications of a Molecular Gas Beam during Electron Beam Induced Deposition. *ACS Appl. Mater. Interfaces* **2014**, *6*, 2987−2995.

(18) Sachser, R.; Reith, H.; Huzel, D.; Winhold, M.; Huth, M. Catalytic Purification of Directly Written Nanostructured Pt Microelectrodes. *ACS Appl. Mater. Interfaces* **2014**, *6*, 15868−15874.

(19) Stanford, M. G.; Lewis, B. B.; Noh, J. H.; Fowlkes, J. D.; Roberts, N. A.; Plank, H.; Rack, P. D. Purification of Nanoscale Electron-Beam-Induced Platinum Deposits via a Pulsed Laser-Induced Oxidation Reaction. *ACS Appl. Mater. Interfaces* **2014**, *6*, 21256−21263.

(20) Begun, E.; Dobrovolskiy, O.; Sachser, R.; Gspan, C.; Plank, H.; Huth, M. Post-Growth Purification of Co Nanostructures Prepared by Focused Electron Beam Induced Deposition. *Nanotechnology***2015**, in print.

(21) Van Oven, J. C.; Berwald, F.; Berggren, K. K.; Kruit, P.; Hagen, C. W. Electron-Beam-Induced Deposition of 3-Nm-Half-Pitch Patterns on Bulk Si. *J. Vac. Sci. Technol., B: Microelectron. Nanometer Struct.—Process., Meas., Phenom.* **2011**, *29*, 06F305.

(22) Van Dorp, W. F.; van Someren, B.; Hagen, C. W.; Kruit, P.; Crozier, P. A. Approaching the Resolution Limit of Nanometer-Scale Electron Beam-Induced Deposition. *Nano Lett.* **2005**, *5*, 1303−1307.

(23) Van Dorp, W. F.; Hagen, C. W.; Crozier, P. A.; Kruit, P. Growth Behavior near the Ultimate Resolution of Nanometer-Scale Focused



DOI: 10.1021/am508052k
*ACS Appl. Mater. Interfaces* 2015, 7, 3289−3297

Electron Beam-Induced Deposition. *Nanotechnology* **2008**, *19*, 225305−225309.
(24) Schmied, R.; Fowlkes, J. D.; Winkler, R.; Rack, P. D.; Plank, H. Fundamental Edge Broadening Effects during Focused Electron Beam Induced Nanosynthesis*Beilstein J. Nanotechnol.***2015**, accepted.
(25) Utke, I.; Friedli, V.; Purrucker, M.; Michler, J. Resolution in Focused Electron- and Ion-Beam Induced Processing. *J. Vac. Sci. Technol., B: Microelectron. Nanometer Struct.—Process., Meas., Phenom.* **2007**, *25*, 2219−2223.
(26) Plank, H.; Smith, D. A.; Haber, T.; Rack, P. D.; Hofer, F. Fundamental Proximity Effects in Focused Electron Beam Induced Deposition. *ACS Nano* **2012**, *6*, 286−294.
(27) Bret, T.; Utke, I.; Hoffmann, P.; Abourida, M.; Doppelt, P. Electron Range Effects in Focused Electron Beam Induced Deposition of 3D Nanostructures. *Microelectron. Eng.* **2006**, *83*, 1482−1486.
(28) Lassiter, M. G.; Rack, P. D. Nanoscale Electron Beam Induced Etching: A Continuum Model That Correlates the Etch Profile to the Experimental Parameters. *Nanotechnology* **2008**, *19*, 455306−455314.
(29) Smith, D. A.; Fowlkes, J. D.; Rack, P. D. Understanding the Kinetics and Nanoscale Morphology of Electron-Beam-Induced Deposition via a Three-Dimensional Monte Carlo Simulation: The Effects of the Precursor Molecule and the Deposited Material. *Small J.* **2008**, *4*, 1382−1389.
(30) van Dorp, W. F.; Lazar, S.; Hagen, C. W.; Kruit, P. Solutions to a Proximity Effect in High Resolution Electron Beam Induced Deposition. *J. Vac. Sci. Technol., B: Microelectron. Nanometer Struct.—Process., Meas., Phenom.* **2007**, *25*, 1603.
(31) Friedli, V.; Utke, I. Optimized Molecule Supply from Nozzle-Based Gas Injection Systems for Focused Electron- and Ion-Beam Induced Deposition and Etching: Simulation and Experiment. *J. Phys. D. Appl. Phys.* **2009**, *42*, 125305.
(32) Szkudlarek, A.; Gabureac, M.; Utke, I. Determination of the Surface Diffusion Coefficient and the Residence Time of Adsorbates via Local Focused Electron Beam Induced Chemical Vapour Deposition. *J. Nanosci. Nanotechnol.* **2011**, *11*, 8074−8078.
(33) Utke, I.; Friedli, V.; Purrucker, M.; Michler, J. Resolution in Focused Electron- and Ion-Beam Induced Processing. *J. Vac. Sci. Technol., B: Microelectron. Nanometer Struct.—Process., Meas., Phenom.* **2007**, *25*, 2219−2223.
(34) Chen, P.; van Veldhoven, E.; Sanford, C. A.; Salemink, H. W. M.; Maas, D. J.; Smith, D. A.; Rack, P. D.; Alkemade, P. F. A. Nanopillar Growth by Focused Helium Ion-Beam-Induced Deposition. *Nanotechnology* **2010**, *21*, 455302.
(35) Alkemade, P. F. A.; Miro, H.; van Veldhoven, E.; Maas, D. J.; Smith, D. A.; Rack, P. D. Pulsed Helium Ion Beam Induced Deposition: A Means to High Growth Rates. *J. Vac. Sci. Technol., B: Microelectron. Nanometer Struct.—Process., Meas., Phenom.* **2011**, *29*, 06FG05.
(36) Van Dorp, W. F.; Wnuk, J. D.; Gorham, J. M.; Fairbrother, D. H.; Madey, T. E.; Hagen, C. W. Electron Induced Dissociation of Trimethyl(methylcyclopentadienyl) Platinum (IV): Total Cross Section as a Function of Incident Electron Energy. *J. Appl. Phys.* **2009**, *106*, 074903.
(37) Wnuk, J. D.; Gorham, J. M.; Rosenberg, S. G.; van Dorp, W. F.; Madey, T. E.; Hagen, C. W.; Fairbrother, D. H. Electron Induced Surface Reactions of the Organometallic Precursor Trimethyl-(methylcyclopentadienyl)platinum(IV). *J. Phys. Chem. C* **2009**, *113*, 2487−2496.
(38) Spencer, J. A.; Rosenberg, S. G.; Barclay, M.; Wu, Y.-C.; McElwee-White, L.; Fairbrother, D. H. Understanding the Electron-Stimulated Surface Reactions of Organometallic Complexes to Enable Design of Precursors for Electron Beam-Induced Deposition. *Appl. Phys. A: Mater. Sci. Process.* **2014**, *117*, 1631−1644.
(39) Winkler, R.; Geier, B.; Plank, H. Spatial Chemistry Evolution during Focused Electron Beam-Induced Deposition: Origins and Workarounds. *Appl. Phys. A: Mater. Sci. Process.* **2014**, *117*, 1675−1688.
(40) Plank, H.; Haber, T.; Gspan, C.; Kothleitner, G.; Hofer, F. Chemical Tuning of PtC Nanostructures Fabricated via Focused Electron Beam Induced Deposition. *Nanotechnology* **2013**, *24*, 175305.
(41) Okazaki, S. High Resolution Optical Lithography or High Throughput Electron Beam Lithography: The Technical Struggle from the Micro to the Nano-Fabrication Evolution. *Microelectron. Eng.* **2015**, *133*, 23−35.
(42) Demers, H.; Poirier-Demers, N.; Couture, A. R.; Joly, D.; Guilmain, M.; De Jonge, N.; Drouin, D. Three-Dimensional Electron Microscopy Simulation with the CASINO Monte Carlo Software. *Scanning* **2011**, *33*, 135−146.


DOI: 10.1021/am508052k
*ACS Appl. Mater. Interfaces* 2015, 7, 3289−3297